

**Key Points:**

- Ion temperature enhancements are frequently observed in the noon sector of the polar cap under interplanetary magnetic field north conditions
- Current models driven by large-scale convection and precipitation fail to produce the observed ion temperature enhancements
- Mesoscale flows and precipitation structures may be critical to account for ion heating in the polar cap

**Supporting Information:**

Supporting Information may be found in the online version of this article.

**Correspondence to:**

L. J. Lamarche,  
leslie.lamarche@sri.com

**Citation:**

Lamarche, L. J., Varney, R. H., & Reimer, A. S. (2021). Ion heating in the polar cap under northwards IMF  $B_z$ . *Journal of Geophysical Research: Space Physics*, 126, e2021JA029155. <https://doi.org/10.1029/2021JA029155>

Received 26 JAN 2021

Accepted 8 OCT 2021

## Ion Heating in the Polar Cap Under Northwards IMF $B_z$

Leslie J. Lamarche<sup>1</sup> , Roger H. Varney<sup>1</sup> , and Ashton S. Reimer<sup>1</sup> 

<sup>1</sup>SRI International, Menlo Park, CA, USA

**Abstract** Joule heating deposits a significant amount of energy into the high-latitude ionosphere and is an important factor in many magnetosphere-ionosphere-thermosphere coupling processes. We consider the relationship between localized temperature enhancements in polar cap measured with the Resolute Bay Incoherent Scatter Radar-North (RISR-N) and the orientation of the interplanetary magnetic field (IMF). Based on analysis of 10 years of data, RISR-N most commonly observes ion heating in the noon sector under northwards IMF  $B_z$ . We interpret heating events in that sector as being primarily driven by sunwards plasma convection associated with lobe reconnection. We attempt to model two of the observed temperature enhancements with a data-driven first principles model of ionospheric plasma transport and dynamics, but fail to fully reproduce the ion temperature enhancements. However, evaluating the ion energy equation using the locally measured ion velocities reproduces the observed ion temperature enhancements. This result indicates that current techniques for estimating global plasma convection pattern are not adequately capturing mesoscale flows in the polar cap, and this can result in underestimation of the energy deposition into the ionosphere and thermosphere.

### 1. Introduction

Joule heating in the polar cap F-region ionosphere is a significant factor in magnetosphere-ionosphere coupling. Magnetic reconnection between the interplanetary magnetic field (IMF) and the Earth's magnetosphere drives strong plasma convection across the entire polar region (Dungey, 1961). A relative velocity between ionized species and neutral species increases collisions between the two and heats both the plasma and neutral populations (Aikio et al., 2012; Fujii et al., 1999; Thayer et al., 1995; Thayer & Semeter, 2004). Plasma temperature enhancements have been connected to ion upflow, which contributes to the outflow of ionospheric plasma into the magnetosphere (Skjæveland et al., 2011; Wahlund et al., 1992). Ion outflow from the polar ionosphere has been identified as a significant source of cold-ion transport into the ring current and plasma sheet (Li et al., 2013; Peterson et al., 2009), resulting in mass loading of the magnetosphere (Li et al., 2012; Moore & Horwitz, 2007).

Joule heating is most significant in the cusp and auroral regions at high-latitudes (Aikio & Selkälä, 2009; Foster & St.-Maurice, 1983; Olsson et al., 2004), however, it has been identified as the dominant form of energy input into the polar cap, particularly during active periods (Lu et al., 2016). Joule heating is estimated to be responsible for 50%–60% of the global storm time energy budget (Knipp et al., 1998; Østgaard et al., 2002; Tanskanen et al., 2002). The IMF orientation can also impact Joule heating at high-latitudes, in addition to broader ion transport processes (Cai et al., 2014; Howarth & Yau, 2008; McHarg et al., 2005; Yau et al., 2012). Extensive statistical surveys of the entire high-latitude region have resulted in empirical models of Joule heating patterns parameterized by IMF conditions and geomagnetic indices (Chun et al., 2002; Palmroth et al., 2005; X. X. Zhang et al., 2005), however, these are mostly useful to gain insight on the average large-scale behavior and are not designed to predict localized heating events.

Time-varying magnetic reconnection at the magnetopause can drive heating events in the ionosphere (Lockwood et al., 2005; Moen et al., 2004). In particular, northwards IMF moves the reconnection point from close to the sun-earth line to the lobe of the magnetosphere, which significantly changes the ionospheric convection pattern (Burke et al., 1979; Cowley, 1983). The resulting pattern often has three or more cells and is highly asymmetric (particularly if there is also a strong IMF  $B_y$  component) (Cousins & Shepherd, 2010; Förster, Haaland, et al., 2008; Reiff & Heelis, 1994; Thomas & Shepherd, 2018). These patterns can cause strong flow channels in the dayside polar cap, which may be responsible for significant localized Joule heating events.

This study will examine localized ion temperature enhancements in the polar cap ionosphere, particularly in relation to IMF conditions known to cause dayside plasma flow channels. In addition to a statistical analysis of ion temperature, we will attempt to model several observed Joule heating events to gain more insight as to what geophysical parameters and processes contribute to localized heating in the polar cap. We will compare global model results with local observations heating events and plasma flows to determine the significance of mesoscale structures.

## 2. Methodology

### 2.1. RISR-N

The Resolute Bay Incoherent Scatter Radar-North (RISR-N) is an Advanced Modular Incoherent Scatter Radar (AMISR) located deep within the northern polar cap (Bahcivan et al., 2010; Kelly & Heinselman, 2009). At 82°N magnetic latitude (74.7°N, 94.9°W geodetic) with a boresight directed roughly toward the magnetic pole, RISR-N is ideally located to observe open field line plasma dynamics. By employing electronic beam steering, RISR-N can quickly cycle through multiple look directions within its field-of-view to measure electron density, ion and electron temperature, and line-of-sight plasma velocity in a 3-D volume in the ionosphere. RISR-N first began collecting science data in 2009 and operated roughly 5–10 days per month between 2009 and 2018. In September 2018, a new smaller generator was installed at the site (in addition to the main generator) to power the radar, which allows much more flexibility in scheduling operations and observation time. One advantage of this has been several month-long periods of almost continuous low duty cycle radar operations since the beginning of 2019.

This study focuses on F-region dynamics so only long-pulse data are presented. The standard AMISR processing routine gates the lag product array into autocorrelation functions, and determines the plasma parameters within each range gate through nonlinear least squares fitting of the autocorrelation functions. This analysis assumes the fitted parameters are slowly varying in range over the pulse length and in time over the integration period. Most standard modes have a range resolution between 49 and 72 km and a minimum integration period of 1–3 min. The data-model comparisons shown later in this study use special Topside modes, which are optimized for observing dynamics in the topside F-region. These topside modes use only five beam positions in order to increase the number of samples in each beam compared to more typical RISR-N modes using 11–52 beam positions. The topside modes interleave long pulses of different lengths, although this manuscript will only discuss parameters derived from the 480  $\mu$ s pulses (72 km range spreading) using the standard AMISR processing.

### 2.2. IPWM

The Ionosphere/Polar Wind model (IPWM) is a 3-D plasma transport model designed for high-latitudes (Varney et al., 2015, 2016). It solves the eight-moment equations for the parallel transport of  $H^+$ ,  $He^+$ ,  $O^+ ({}^4S)$ , and electrons. Photochemistry for the species  $N^+$ ,  $NO^+$ ,  $N_2^+$ ,  $O_2^+$ ,  $O^+ ({}^2D)$ , and  $O^+ ({}^2P)$  is also included. The model includes a kinetic electron solver, but it has been disabled for the simulations done in this study. The parallel dynamics solver in IPWM uses time-splitting to separate the transport from the chemistry and conduction. The transport portion uses a conservative explicit finite volume scheme with second-order van Leer flux limiters (Varney et al., 2014). An implicit Euler scheme is used for the stiff terms associated with chemistry, collisions, and electron heat conduction along the field line. The perpendicular transport is a conservative finite volume advection scheme using second-order van Leer flux limiters and specified  $E \times B$  drifts (Varney et al., 2015). IPWM takes the density and temperature of neutral species from the Naval Research Laboratory's Mass Spectrometer Incoherent Scatter Radar Extended (NRLMSISE-00) empirical model (Picone et al., 2002). NRLMSISE-00 is driven by the F10.7 solar radio flux, a proxy for solar extreme ultraviolet radiation, and the Ap geomagnetic index. Neutral winds are provided by the High-Latitude Thermospheric Wind Model (HL-TWiM) (Dhadly et al., 2019). HL-TWiM is an empirical model of F-region neutral winds based on several decades of high-latitude ground-based and space-based measurements, including Fabry-Perot Interferometer measurements from an instrument at the Resolute Bay Observatory. The solar EUV spectra is provided by a high-resolution solar EUV irradiance model for aeronomic

calculations (HEUVAC) (Richards et al., 2006). The model calculates production and heating from precipitation with the empirical relationships described in Fang et al. (2008).

IPWM uses a nonorthogonal magnetic-centered dipole Eulerian grid. The grid is constructed from surfaces of constant  $L$  shell, MLT, and altitude. The lower boundary is set at 97 km by chemical equilibrium while the upper boundary is open at 8,400 km. The equatorward boundary (set at  $L = 4$ ) is treated as a hard wall with no transport from lower latitudes. All simulations shown in this paper use a spatial resolution of approximately 110 km in latitude by 200 km in longitude. More specifically, the model uses  $1^\circ$  spacing in invariant latitude and a variable resolution longitude grid that progressively halves the resolution moving inwards toward the pole to avoid excessive resolution near the pole. The longitude grid has 128 points ( $2.8125^\circ$  resolution) equatorward of  $68^\circ$  invariant latitude, 64 points ( $5.625^\circ$  resolution) between  $68^\circ$  and  $80^\circ$  invariant latitude, and 32 points ( $11.25^\circ$  resolution) poleward of  $80^\circ$  invariant latitude. The IPWM inputs are specified at 1 min resolution and IPWM outputs are stored at 1 min resolution, although the internal timesteps are much shorter and determined by a Courant condition.

IPWM requires high-latitude energetic particle precipitation and electrostatic potential patterns as inputs. Past work with IPWM has always used magnetospheric simulations to set these inputs (Varney et al., 2016). In contrast, in this work, simulations will be driven by precipitation patterns derived from the Ovation Prime empirical model (Newell et al., 2009). Ovation Prime outputs the number flux and average energy of monoenergetic and broadband precipitation for a requested magnetic latitude and MLT at high-latitudes. The model is based on data from the DMSP SSJ/4 electrostatic analyzers (Hardy et al., 1984, 2008) and is parameterized by solar wind conditions.

Electrostatic potential patterns are derived from SuperDARN convection maps. The Super Dual Auroral Radar Network (SuperDARN) consists of about 30 ground-based high-frequency coherent-scatter radars at midlatitudes, high-latitudes, and polar latitudes (Chisham et al., 2007; Greenwald et al., 1995; Nishitani et al., 2019). Each radar makes independent line-of-sight measurements of the plasma velocity, but convection maps covering the entire polar region can be created by combining all measurements from a particular time with a climatological model of convection patterns based on geophysical parameters such as the IMF and dipole tilt angle (Cousins & Shepherd, 2010; Greenwald et al., 1995; Thomas & Sheperd, 2018). The convection patterns used here were formed from real SuperDARN measurements assimilated with the Ruohoniemi and Greenwald (1996) statistical model. This method uses an eighth-order spherical harmonic fit and generates a new convection pattern every two minutes. At present, this is the standard SuperDARN convection map data product. In the events considered in this paper, individual SuperDARN radars had good backscatter coverage in the region immediately around Resolute Bay, so we are reasonably confident the convection patterns are accurate in the local comparison region. SuperDARN convection maps are available on a  $1^\circ$  magnetic latitude by  $2^\circ$  magnetic longitude grid, which is comparable to the native IPWM grid in the relevant regions, so interpolation errors should be minimal.

### 3. Results

#### 3.1. Statistical Analysis of Ion Temperature Enhancements

We performed a statistical analysis of ion temperature over the entire RISR-N database in order to determine which conditions most commonly produced ion heating. The database consists of all 5-min-integrated long-pulse data collected by RISR-N between January 2010 and February 2020. For each experiment, we filter out points where the AMISR fitting procedure is expected to have failed or where the ion temperature error exceeds 1,000 K. Failed fits are detected by checking if the exit code from the Levenberg-Marquardt algorithm, which performs the nonlinear least squares fitting, does not indicate successful convergence, or if the normalized chi-square statistic is less than 0.1 or greater than 10. Then we extract the median ion temperature between 300 and 400 km altitude in the highest elevation beam within the grating lobe limit of the radar's field-of-view. Above 300 km, the AMISR fitting procedure assumes the ion composition is entirely O<sup>+</sup>. For experiments where the database does not include 5-min-integrated files, we postintegrate higher-cadence data to 5 min by taking an error weighted average in time after the initial "failed fit" filter, then removing any points where the resulting weighted ion temperature error is greater than 1,000 K before finding the median temperature between 300 and 400 km altitude. After extracting the median F-region ion

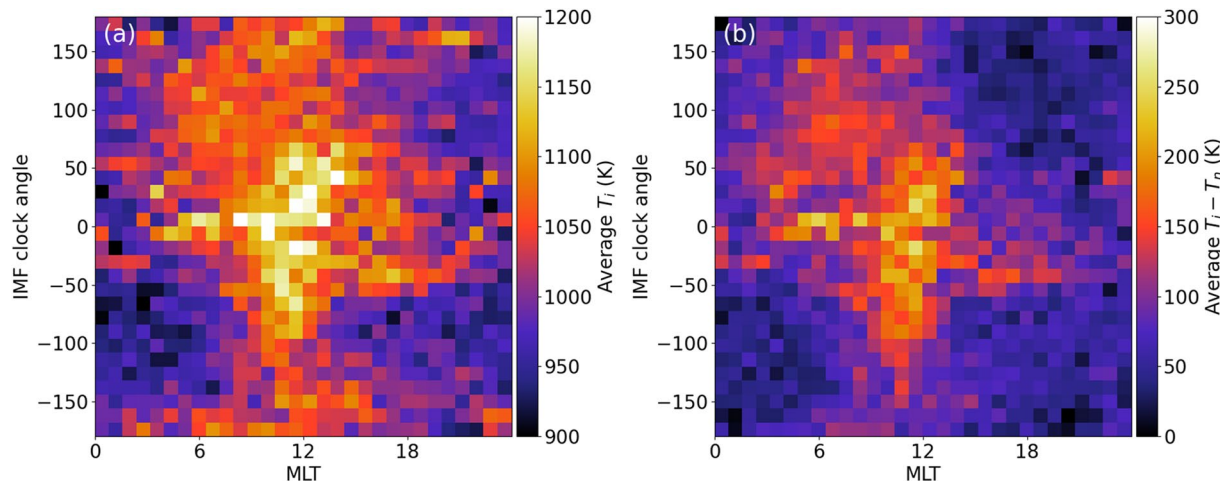


**Figure 1.** (a) Bin-averaged ion temperature observed by Resolute Bay Incoherent Scatter Radar-North (RISR-N) per MLT sector and interplanetary magnetic field (IMF) clock angle, and (b) bin-average ion temperature minus NRLMSISE-00 neutral temperature per MLT sector and IMF clock angle. A clock angle of zero indicates northwards IMF.

temperature for every long-pulse experiment, we bin these data by magnetic local time (0.8 h bins) and the IMF clock angle (12° bins) using 1-h resolution OMNI data and calculate the average temperature in each bin. The results are plotted in Figure 1a. Note that the IMF clock angle is defined as  $\theta_c = \arctan(B_y/B_z)$  such that  $\theta_c = 0^\circ$  corresponds to the IMF directed northwards. In order to detrend diurnal, seasonal, and solar cycle variations in the neutral atmosphere, we have also computed the average of  $(T_i - T_n)$  using neutral temperatures,  $T_n$ , from NRLMSISE-00 (Picone et al., 2002).

Figure 1a shows that on average, RISR-N observes higher ion temperatures in the noon sector, particularly when the IMF has a significant northwards component ( $\theta_c = 0^\circ$ ). Furthermore, Figure 1b demonstrates that this pattern persists even after subtracting the neutral temperature. At 12 MLT, RISR-N is located just polewards of the cusp (B. Zhang et al., 2013). This region often experiences fast plasma flows, particularly under northwards IMF conditions when magnetic reconnection occurs in the lobe of the magnetosphere driving four-cell or asymmetric convection patterns in the ionosphere. It should be clarified that these are flows in the polar cap and not associated with the bursty reconnection flows that occur in the cusp (Farrugia et al., 2004; Prikryl et al., 2002; Provan et al., 2002). The elevated average ion temperature observed under these conditions may be due to an increased likelihood of RISR-N observing a Joule heating event due to fast sunward flows in the plasma driven by lobe reconnection.

To test the theory that fast flows on the dayside during northwards IMF conditions are responsible for the temperature enhancements seen in Figure 1, we plot the average magnitude of the ion drift velocity,  $|\vec{V}_i|$ , and the average magnitude of the ion velocity relative to the neutral,  $|\vec{V}_i - \vec{V}_n|$ , in the same format (Figures 2a and 2b, respectively). The full ion drift velocity vector is inverted from line-of-sight velocity measurements from different RISR-N beams using the Bayesian inversion technique described in Heinselman and Nicolls (2008). Neutral velocity vectors are taken from HL-TWiM (Dhadly et al., 2019). The velocity vector inversion was performed on all processed experiments in the RISR-N database. Data from all 5-min experiments, as well as higher-cadence experiments that were postintegrated to 5-min after the vector inversion process, are included in Figure 2.

In almost all regions of Figure 2 (including the large enhancement around 6 MLT and  $\theta_c = 120^\circ$ ),  $|\vec{V}_i - \vec{V}_n|$  (Figure 2b) is less than  $|\vec{V}_i|$  (Figure 2a). This is consistent with  $\vec{V}_i$  and  $\vec{V}_n$  being oriented in a similar direction so the vector subtraction reduces the resulting magnitude. The notable exception to this occurs at 12 MLT under northwards IMF, where  $|\vec{V}_i - \vec{V}_n| > |\vec{V}_i|$ , indicating  $\vec{V}_n$  opposes  $\vec{V}_i$ . We can confirm this by considering similar plots of the east and north components of the ion and neutral velocities (Figure 3). This uses the same ion and neutral velocities as Figure 2. Figures 3a and 3b show the ion velocity eastwards ( $V_{iE}$ ) and northwards ( $V_{iN}$ ) components, respectively. Figures 3c and 3d show the neutral velocity eastwards ( $V_{nE}$ ) and northwards ( $V_{nN}$ ) components, respectively. The patterns in Figure 3 agree with the standard notion of

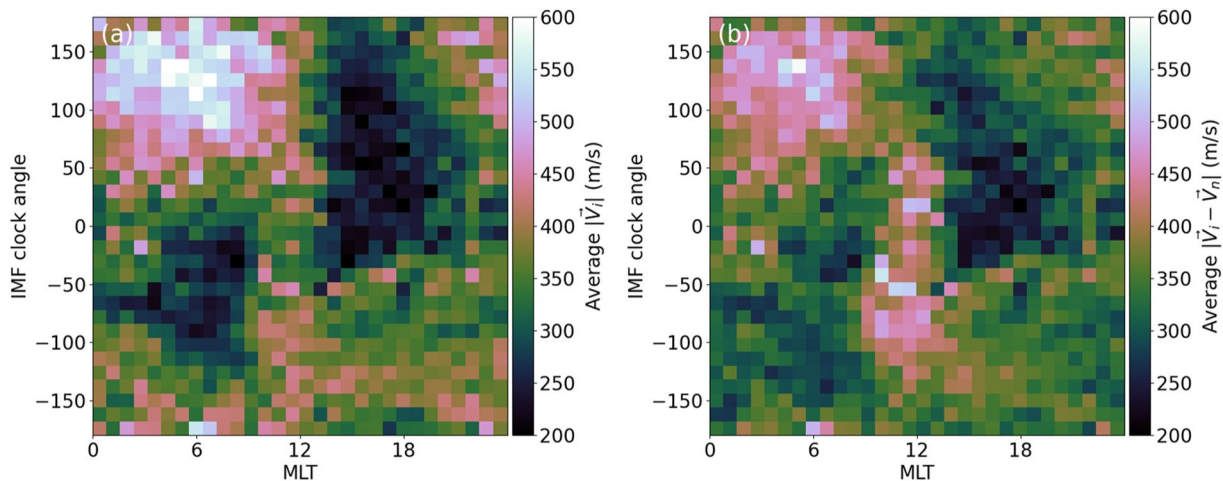


**Figure 2.** (a) Average magnitude of the ion velocity observed by Resolute Bay Incoherent Scatter Radar-North (RISR-N) per MLT sector and interplanetary magnetic field (IMF) clock angle, and (b) average magnitude of the ion velocity minus High-Latitude Thermospheric Wind Model (HL-TWiM) neutral wind velocities per MLT sector and IMF clock angle. A clock angle of zero indicates northwards IMF.

IMF-dependent two-cell or four-cell convection patterns. Note how in Figure 3a at 6 MLT and  $\theta_c = 120^\circ$ ,  $\vec{V}_i$  has a strong westwards component (corresponding to the similar enhancement in Figure 2a), but because  $\vec{V}_n$  is also predominantly westwards (Figure 3c), the resulting difference magnitude decreases (Figure 2b). Conversely, at 12 MLT and  $\theta_c = 0^\circ$ ,  $\vec{V}_i$  is equatorwards (Figure 3b) while  $\vec{V}_n$  is polewards (Figure 3d), resulting in the enhancement seen in Figure 2b and the corresponding amplified average ion temperatures in that sector noted in Figure 1. This supports the idea that ion temperature enhancements are common in the noon sector under IMF northwards conditions, and that they are related to the IMF driving a plasma convection pattern that contains localized sunwards flows that oppose the background neutral velocity.

The RISR-N database contains several large heating events at local times away from 12 MLT, many of which are directly related to large geomagnetic storms. Most of these storm events, however, end up being statistical outliers in their particular MLT and IMF clock angle bin. Note that our analysis only sorts by IMF clock angle, and not IMF magnitude. The few storm events with very large IMF magnitude and southwards clock angle do show elevated ion temperatures, but the relatively rarity of those events results in them not significantly contributing to the averages in Figure 1. The enhancement at 12 MLT and  $\theta_c = 0^\circ$  in Figures 1 and 2 indicate that fast flow and heating events under those conditions are very common and are not confined to geomagnetic storm times.

### 3.2. Modeling Joule Heating Events With IPWM

We chose two particularly large ion heating events observed by RISR-N for detailed case studies: one in May 2014 and another in April 2016. During these events, RISR-N observed strong temperature enhancements, the SuperDARN backscatter coverage in the vicinity of RISR-N was reasonable, and the convection pattern exhibited dayside reverse convection cells resulting in sunwards flows. The May 2014 event has been previously discussed by Shen et al. (2016), and it was also a large ion upflow event observed by the enhanced Polar Outflow Probe (e-POP). Both of these events occurred during while the IMF had a northwards component and both were observed using topside modes at RISR-N. These events both have ion temperatures significantly higher than the average ion temperatures in Figure 1, but neither is as extreme as the September 2014 event previously discussed by Clauer et al. (2016). Animations of full runs are provided in Movies S1 and S2.

Figure 4 summarizes the heating observations and simulation results from the May 2014 event. Figure 4a shows the high-resolution (5 min cadence) OMNI IMF By and Bz components during this event. Note that while high-resolution data are shown for context, the low resolution 1 h average OMNI data were used to drive all models used in this study. Because plasma convection does not respond instantaneously to changes

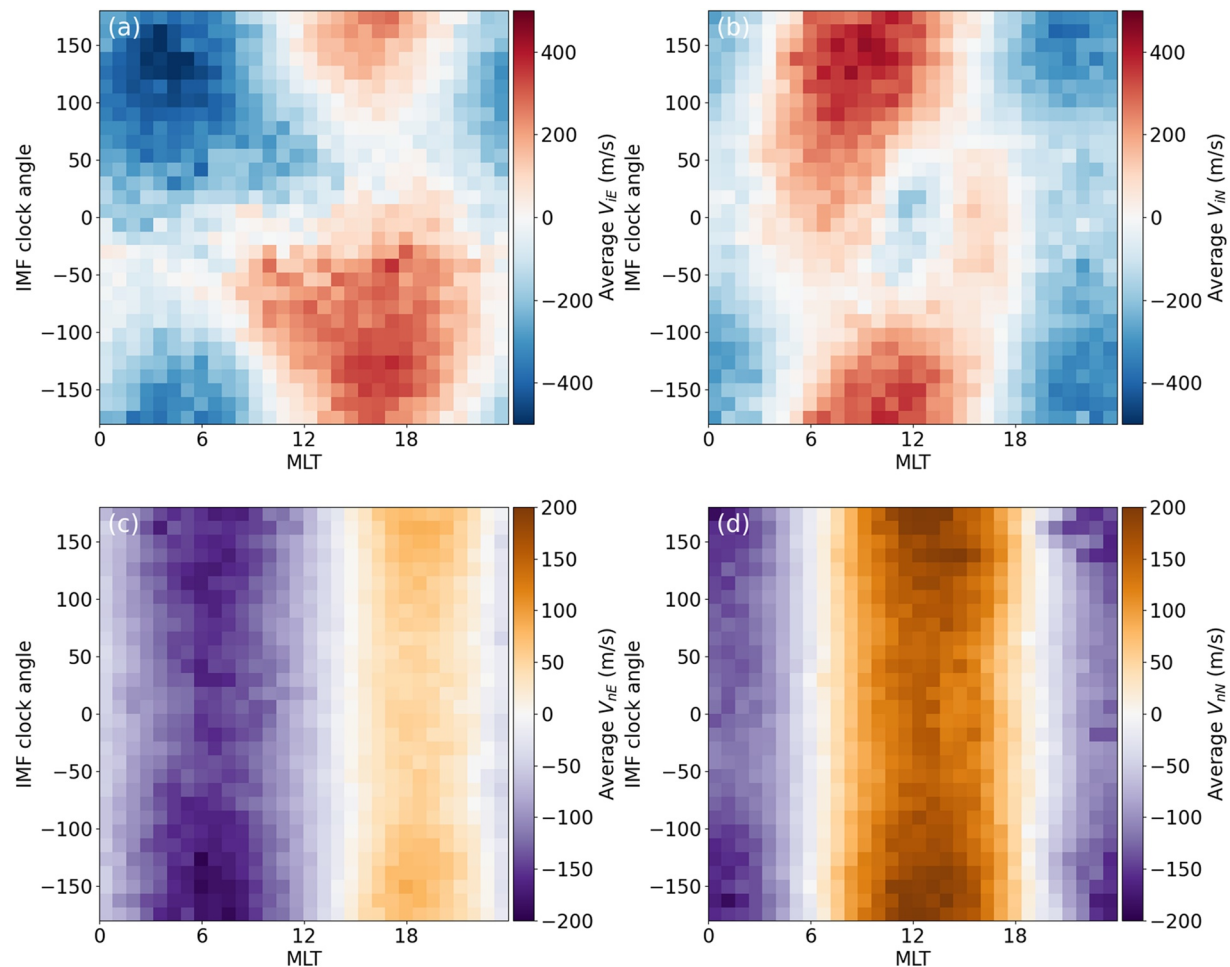


**Figure 3.** (a) Average eastwards component of the ion velocity observed by Resolute Bay Incoherent Scatter Radar-North (RISR-N) per MLT sector and interplanetary magnetic field (IMF) clock angle, (b) average northwards of the ion velocity observed by RISR-N per MLT sector and IMF clock angle, (c) average eastwards component of the neutral velocity from the High-Latitude Thermospheric Wind Model (HL-TWiM) per MLT sector and IMF clock angle, and (d) Average northwards component of the neutral velocity from HL-TWiM per MLT sector and IMF clock angle. A clock angle of zero indicates northwards IMF.

in the IMF, it is appropriate to use hourly averages to characterize the convection patterns. Figures 4b and 4c show ion temperature modeled in the field line grid cell closest to Resolute Bay and measured in the RISR-N beam closest to vertical ( $80^\circ$  elevation), respectively. The data are presented in universal time (UT), and at RISR-N  $\text{MLT} = \text{UT} - 6$ , such that noon is 18 UT. The RISR-N measurements in Figure 4c show two strong ion temperature enhancements on May 30, 2014, a broad one around 21 UT and a shorter but more intense one right before 22 UT. Figure 5 is a snapshot of the IPWM ion convection, neutral wind, and particle precipitation drivers, as well as the output ion temperature from IPWM at 300 km at May 30, 2014 21:50 UT. All panels are in the native IPWM dipole grid with gray dashed lines showing dipole colatitude  $10^\circ$  and  $20^\circ$  off the pole. The location of RISR-N is indicated with a black tripod. The northwards IMF  $B_z$  component restructured the ionospheric convection to produce a reverse convection cell near RISR-N. During this observed heating period, IPWM generates some temperature enhancement, but it is substantially less than that measured by RISR-N.

Figure 6 summarizes the heating observations and simulation results of the April 2016 event in the same format as Figure 4. The RISR-N observations in Figure 6c show two distinct heating events: a short one on April 21, 2016 around 19 UT and a much more extended event on April 22, 2016 between 17 and 20 UT. IPWM does not reproduce the short temperature enhancement on April 21, 2016, however it does show some evidence of enhanced ion temperatures during the longer heating event on the next day. Figure 7 is a single snapshot of the IPWM drivers and output on April 22, 2016 at 19:00 UT (following the same format

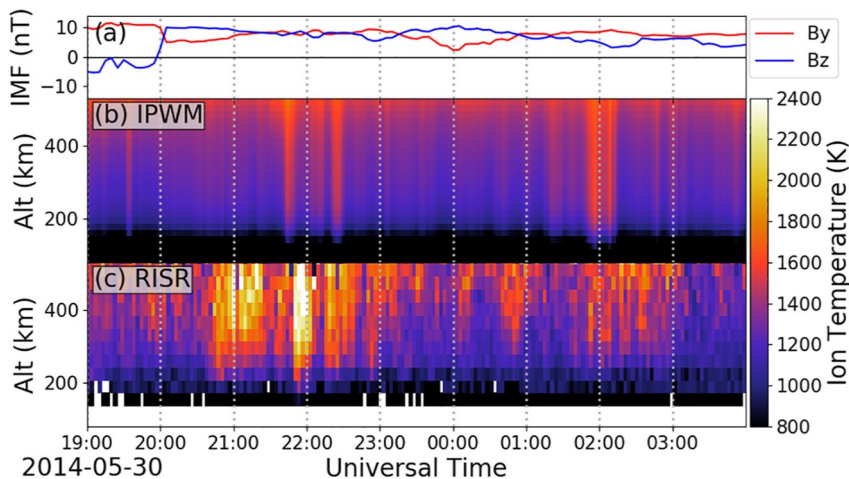


**Figure 4.** Modeled and observed ion temperature over Resolute Bay from May 30, 2014 19:00 UT to May 31, 2014 4:00 UT. Panel a shows the high-resolution (5 min) OMNI IMF By and Bz components. Panel (b) shows the temperature modeled by the Ionosphere/Polar Wind model (IPWM) driven by Ovation Prime precipitation and SuperDARN electric potential maps. Panel (c) shows the ion temperature measured by Resolute Bay Incoherent Scatter Radar-North (RISR-N) along the highest elevation beam.

as Figure 5). During this longer event, the IMF was northwards, but also had a significant By component, resulting in multicelled and highly asymmetric convection patterns. A small temperature enhancement is seen in the IPWM ion temperature at 19 UT (Figure 6b). As seen in Figure 7, this corresponds to a small region of dayside sunwards convection, which is related to an ion temperature enhancement in the vicinity of RISR-N. In this case, the IMF is pointed almost entirely in the positive y direction, resulting in strong downward convection over RISR-N. It is important to note however that IPWM did not fully produce the duration or amplitude of the ion temperature enhancement observed in the RISR-N data for either event considered.

#### 4. Discussion

In the simulations shown in Section 3.2, IPWM is driven with measured convection patterns from SuperDARN and statistical precipitation patterns from Ovation Prime, yet strongly underestimate the observed ion temperature enhancements. This suggests that there are either fundamental physics that are not being captured by IPWM or that these observation-based drivers do not adequately capture all important scales.

SuperDARN is a large-scale network and generally does not provide convection measurements with sufficient spatial resolution to characterize small and mesoscale flows across the entire polar cap. While it is sometimes possible to recover mesoscale structuring from SuperDARN and other networks using sophisticated inversion techniques (Bristow et al., 2016), these data products are generally nonstandard and not available for all times. More advanced convection mapping techniques should be explored in future work. As a first step, it would be interesting to regenerate global SuperDARN convection maps by modifying certain parameters, such as the choice of background statistical model, the order of the spherical harmonic fit, or the temporal resolution of the input OMNI data, to attempt to better resolve mesoscale flows. Small and mesoscale flows may be a significant source of heating in the polar cap ionosphere, contributing to the substantial temperature enhancements shown in Figures 4c and 6c. Chen and Heelis (2018) tabulated a significant number of mesoscale (100–500 km) flow perturbations over the background convection and concluded they were an additional source of frictional heating. In order to assess the importance of mesoscale fast flows in our two events, we examined the local 3-D ion drift velocities from RISR-N (Heinselman & Nicolls, 2008), and approximate the related ion temperature enhancements (Figures 8 and 9).

In the F-region, Equation 1 is a reasonable approximation of the ion energy equation (St.-Maurice & Hanson, 1982).

$$\tilde{T}_i = T_n + \frac{m_n}{3k_B} \left| \vec{V}_i - \vec{V}_n \right|^2 \quad (1)$$

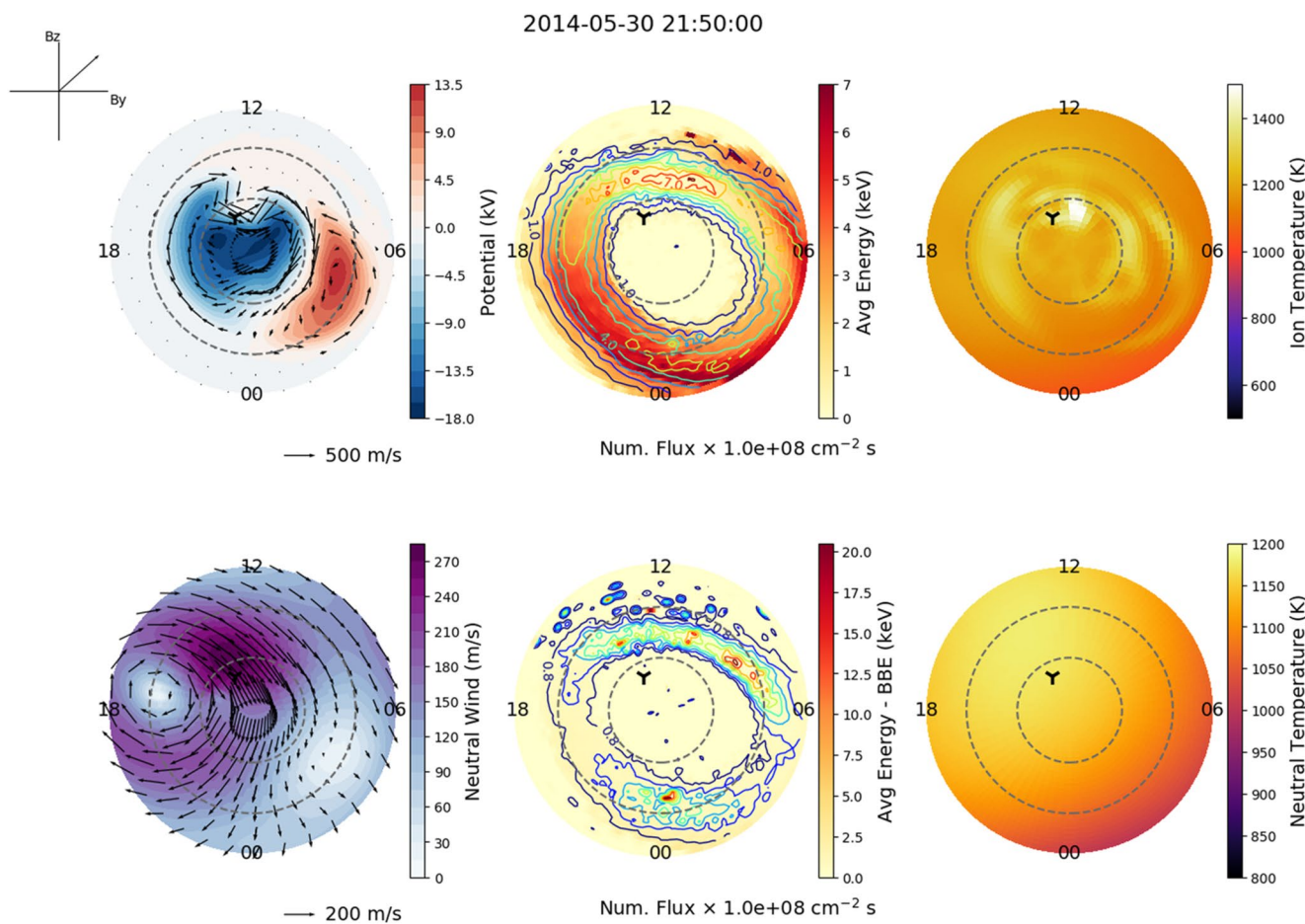
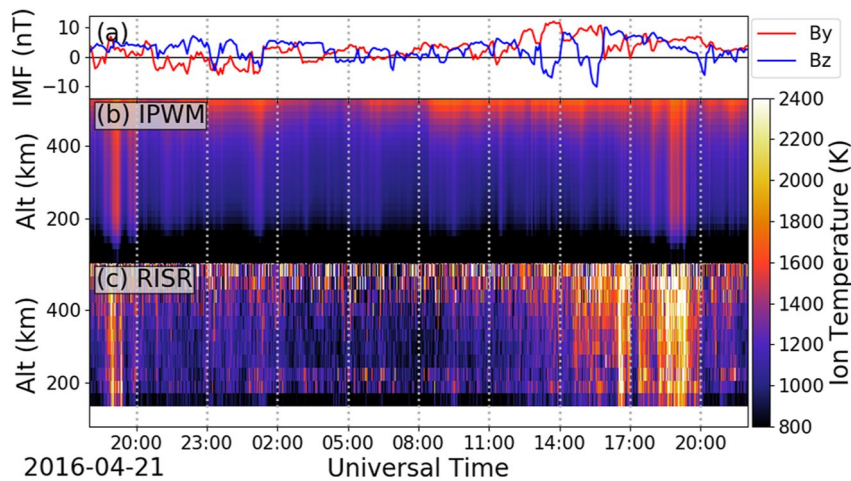


**Figure 5.** Snapshot of the Ionosphere/Polar Wind model (IPWM) run on May 30, 2014 at 21:50 UT. The left column shows the SuperDARN electric potential used to drive IPWM (top) and the background average neutral winds from the High-Latitude Thermospheric Wind Model (HL-TWiM, bottom). The quivers show the ion and neutral velocity fields, respectively, while the background color in the top plot is the electric potential (top) and magnitude of the neutral winds (bottom). The middle plot shows the average energy (background color) and number flux (overlaid line contours) of the input monoenergetic (top) and broadband (bottom) particle precipitation from Ovation Prime. The right panel shows the modeled ion temperatures (top) and neutral temperatures (bottom) at 300 km. All panels are in the IPWM magnetic latitude/MLT grid. The two dashed gray circles indicate magnetic latitude 10° and 20° from the pole. The black tripod shows the location of Resolute Bay Incoherent Scatter Radar-North (RISR-N) in each panel. The hourly average IMF clock angle at this time is indicated in the top left corner.

Here,  $\tilde{T}_i$  and  $T_n$  are the ion and neutral temperatures, respectively,  $m_n$  is the average mass of the neutral species,  $k_B$  is Boltzmann's constant, and  $\vec{V}_i$  and  $\vec{V}_n$  are the ion and neutral velocities, respectively. Although this expression describes frictional heating, Joule heating rates are equivalent to frictional heating rates under F-region assumptions (Thayer & Semeter, 2004). To first order in the F-region, the ion temperature is predominantly determined by the ion-neutral velocity difference. For clarity, we will use  $T_i$  to refer to ion temperature as measured by RISR-N or extracted from IPWM output and  $\tilde{T}_i$  to refer to the expected ion temperature calculated from Equation 1.

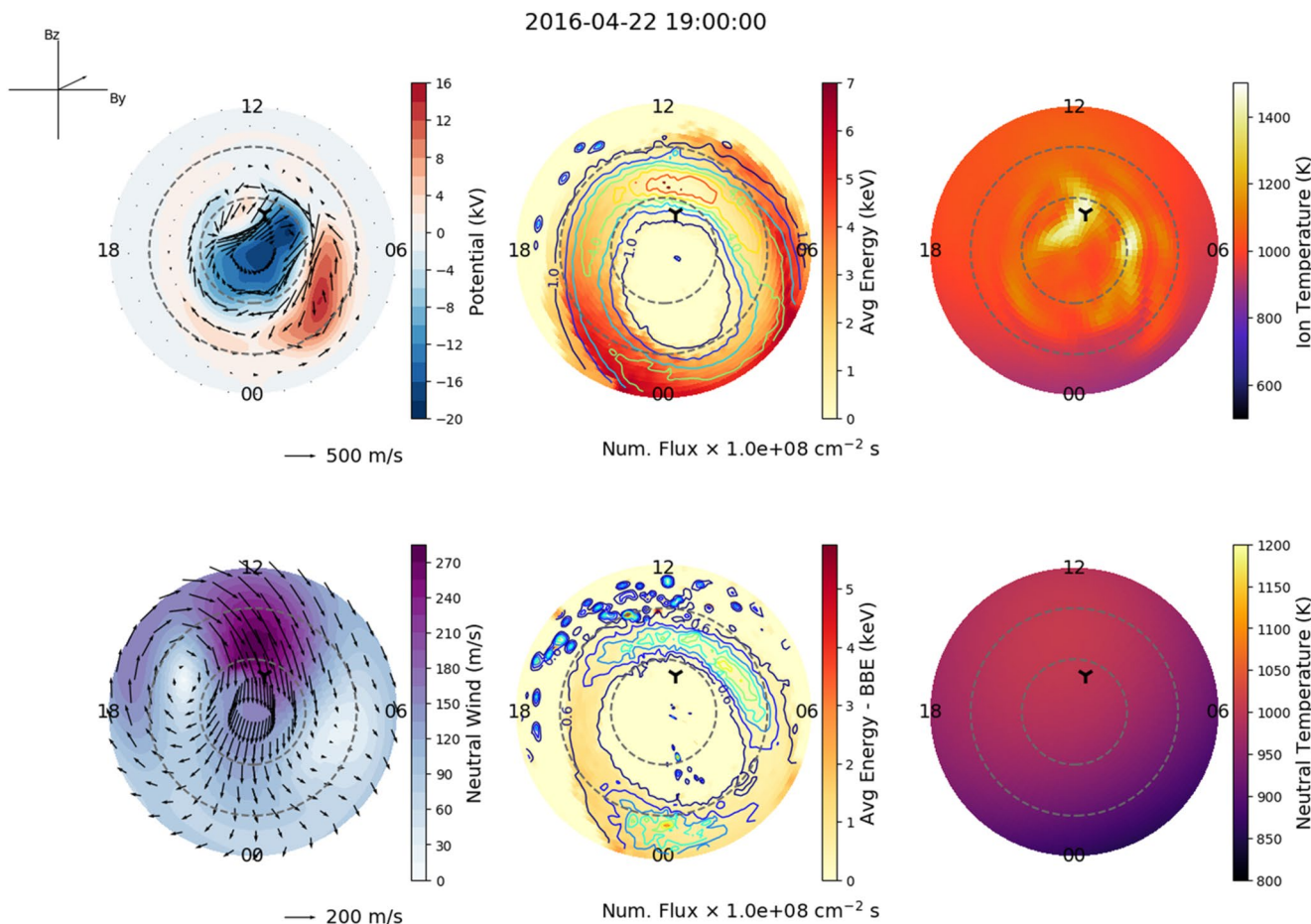
In order to test the consistency of the RISR-N observed temperature enhancements with the locally measured  $\vec{V}_i$ , we have evaluated Equation 1 using the  $\vec{V}_i$  resolved from RISR-N measurements (Heinselman & Nicolls, 2008) and empirical models for  $T_n$  and  $\vec{V}_n$ . The neutral temperatures,  $T_n$  are taken from NRLM-SISE-00 (Picone et al., 2002) and the neutral winds  $\vec{V}_n$  from HL-TWiM (Dhadly et al., 2019).

Figure 8a shows the geodetic eastwards components of the RISR-N ion velocity (blue), the SuperDARN ion velocity (red), and the HL-TWiM neutral velocity (green) at 300 km over Resolute Bay for the May 2014 event. Likewise, Figure 8b shows the geodetic northwards components of these velocities. Figure 8c shows the ion temperature calculated from Equation 1,  $\tilde{T}_i$ , at 300 km using ion velocity from SuperDARN (red) and



**Figure 6.** Modeled and observed ion temperature over Resolute Bay from April 21, 2016 18:00 UT to April 22, 2016 22:00 UT. Figure format same as Figure 4.

RISR-N (blue). It also shows the actual output ion temperature from IPWM (pink) and measured ion temperature from RISR-N (light blue). Figures 8d and 8e show the full temperature,  $\tilde{T}_i$ , profile calculated over Resolute Bay using the RISR-N  $\vec{V}_i$  and the SuperDARN  $\vec{V}_i$ , respectively. Of the parameters that contribute



**Figure 7.** Snapshot of SuperDARN-driven IPWM run on April 22, 2016 at 19:00 UT. Figure format is the same as Figure 5.

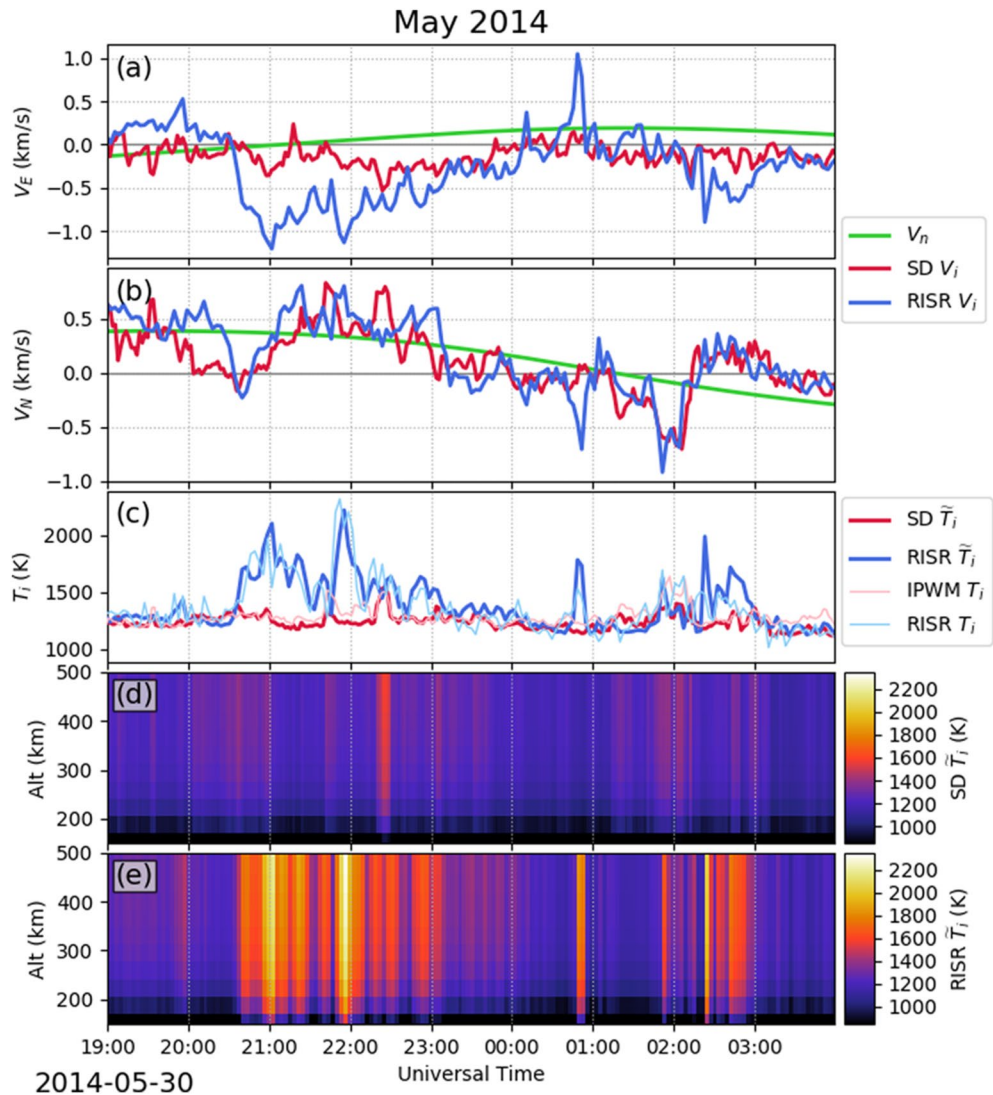


**Figure 8.** Comparison of the ion temperature ( $\tilde{T}_i$ ) calculated from RISR-N and SuperDARN velocities with Equation 1 with the actual observed/modeled ion temperature for the May 2014 heating event. Panels a and b show the geodetic eastwards and northwards (respectively) components of the neutral wind ( $\vec{V}_n$ , green), SuperDARN ion drift ( $\vec{V}_i$ , red), and the RISR-N ion drift ( $\vec{V}_i$ , blue) at 300 km. Panel c shows the ion temperature calculated with Equation 1 at 300 km from the SuperDARN (red) and RISR-N (blue) velocities. For comparison, the IPWM output ion temperature (pink) and RISR-N measured ion temperature (light blue) are also shown. Panels d and e show the full temperature profile calculated with Equation 1 using the SuperDARN and RISR-N ion velocities (respectively) and HL-TWiM neutral winds.

to  $\tilde{T}_i$  in Equation 1,  $T_n$  (from NRLMSISE-00) typically increased with altitude, but  $\vec{V}_n$  (from HL-TWiM) is assumed constant in this altitude range and  $\vec{V}_i$  changes minimally, mapping along the field line as described in Laundal and Richmond (2017). Figure 9 shows the same calculations for the April 2016 event in the same format as Figure 8. In both events, RISR-N locally observed faster ion velocities than predicted by the SuperDARN convection patterns during the heating events (Figures 8a, 8b, 9a and 9b). Furthermore, the ion temperature calculated from Equation 1 with RISR-N mesoscale flows (Figures 8c and 9c, blue lines) matches the measured temperature enhancements (Figures 8c and 9c, light blue lines) substantially better than the IPWM runs (Figures 8c and 9c, pink lines). This can also be seen in how Figure 8e (9e) matches Figure 4c (6c) much more closely than Figure 4b (6b) does.

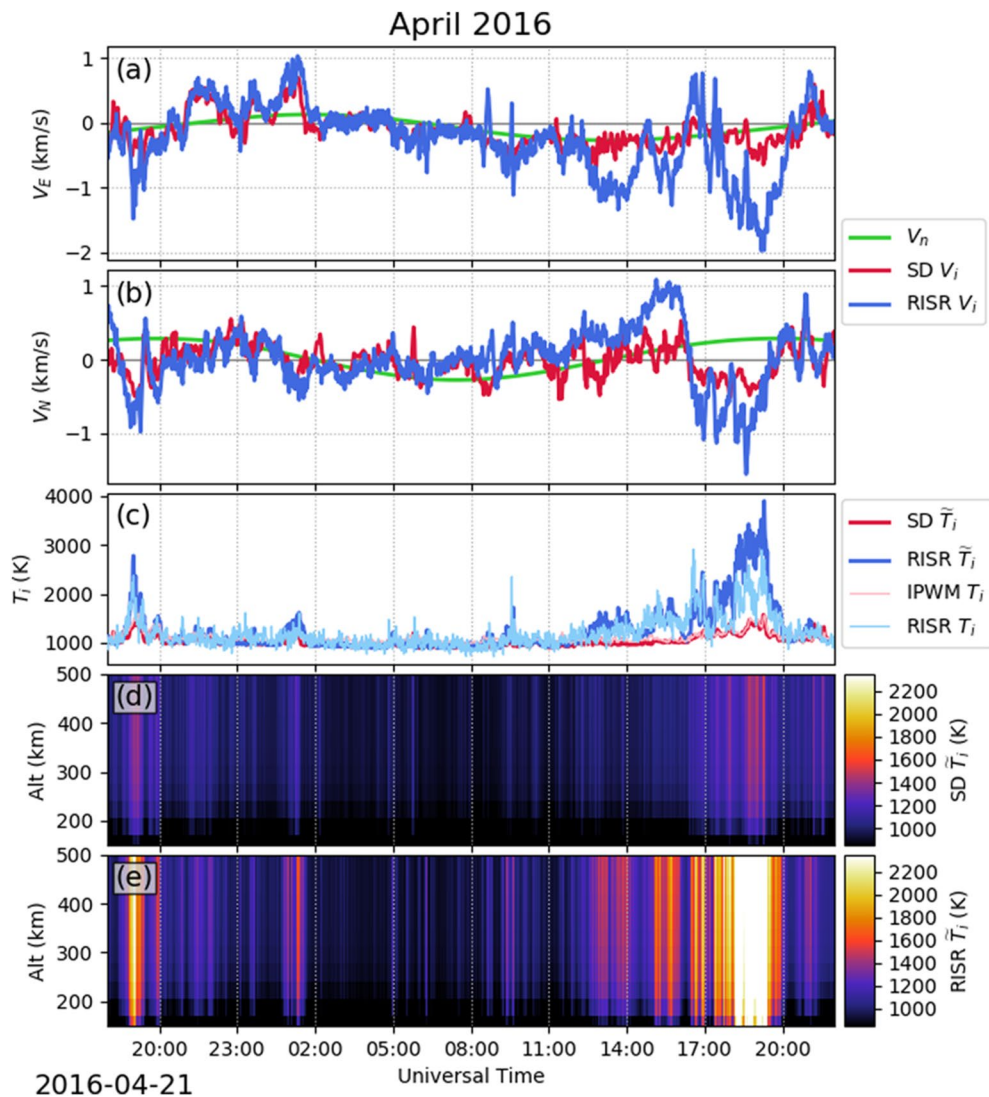


**Figure 9.** Comparison of calculated ion temperatures and observed ion temperatures for the April 2016 heating event. Figure format same as Figure 8.

The underestimation of the ion temperatures in the IPWM simulations can be largely explained by the underestimation of the input ion velocities. IPWM is solving a much more complex ion energy equation than Equation 1, which includes heat conduction along the field lines and ion-electron heating. Nonetheless, we can verify that Equation 1 is a reasonable approximation for the F-region solutions in IPWM. Figures 8c and 9c show the ion temperature calculated using the SuperDARN velocities with Equation 1 (red lines) and the ion temperatures output from IPWM (pink lines). The general agreement between these two lines suggests that the lower IPWM temperatures are in fact consistent with the lower velocities produced by the SuperDARN convection patterns and that the mesoscale flow channels RISR-N observed during these heating events are critical to extreme heating events.

Previous studies have shown good agreement between the SuperDARN and RISR-N line-of-sight velocities (i.e., Koustov et al., 2016); however, there have rarely been comparisons specifically of strong flow events ( $\geq 1$  km/s) like the ones that drove the heating events shown in Figures 8 and 9. Furthermore, the SuperDARN electric potential patterns that were fed into IPWM are designed to be global-scale maps that show dynamics across the entire polar cap, and may struggle to reproduce extremely localized structures like the ones observed by RISR-N during these heating events.

This study uses neutral winds from the HL-TWiM empirical model due to the sparsity of full vector neutral wind measurements in the polar cap. A nonzero neutral wind will reduce the heating rate if the neutral motion is aligned with the ion motion and enhance it if it opposes it (as seen in Figures 1 and 2). As seen in the left-hand column of Figure 7, the ion temperature enhancement modeled over RISR-N is colocated with a region where the neutral velocity opposes the ion velocity. Over a sustained period, strong plasma velocity can drag the neutral atmosphere into a similar pattern through ion-neutral collisions (Emmert et al., 2006; Förster, Rentz, et al., 2008; Richmond et al., 2003). These effects would not be captured by an empirical model like HL-TWiM. Billett et al. (2019) estimated the neutral wind response time to a change in plasma convection at high-latitudes to be roughly 75–90 min, depending on the strength of the event. Consequently, ion heating events may be more common when the IMF is highly variable and the convection pattern is frequently reconfigured. Neither IPWM nor the approach of calculating  $\tilde{T}_i$  with Equation 1 can demonstrate this effect without direct neutral wind measurements.

In addition to subgrid flows, small-scale precipitation structures may also be important to localized heating events. Precipitation can modify the ionospheric conductivity profile, altering how effective Joule heating is at different altitudes. Ovation Prime is a purely empirical model, meaning that unlike the SuperDARN convection data, it does not assimilate real measurements from a particular time so spectral characteristics are based exclusively off of historical statistics. In our simulations, RISR-N is consistently poleward of the large precipitating fluxes in the cusp and in a region where Ovation Prime predicts very little precipitation. The highly structured and dynamic nature of the polar cap in general presents a significant challenge to statistical models, but it is difficult to quantify the uncertainty between the model output and the true precipitation patterns. Northwards IMF conditions, such as those examined in this study, have been associated with sun-aligned arcs, which are known to contain mesoscale precipitation features (L. Zhu et al., 1997). Mesoscale precipitation features of scales not captured by Ovation Prime do impact Joule heating in the auroral zone (Kosch et al., 2011; Q. Zhu et al., 2018), but more research is required to determine if they have a similar effect in the polar cap.

Finally, the thermodynamic ion temperature is the second moment of the full 3-D ion distribution function, whereas monostatic incoherent scatter radars can only measure the 1-D marginal ion distribution function along the radar's line of sight (Akbari et al., 2017). Standard AMISR fitting assumes an isotropic Maxwellian distributions of both electrons and ions, in which case the 1-D line of sight temperatures are the same as the full 3-D ion distribution function. This assumption starts to break down under strong relative ion-neutral drift, which can cause the distribution function to migrate from the assumed isotropic distribution toward an anisotropic bi-Maxwellian or toroidal distribution (St.-Maurice & Schunk, 1979; St.-Maurice & Schunk, 1977). For a bi-Maxwellian distribution with different parallel and perpendicular ion temperatures,  $T_{\parallel i}$  and  $T_{\perp i}$ , the ISR spectrum measured along a line-of-sight at an angle  $\alpha$  away from the magnetic field will be identical to the ISR spectrum from an isotropic Maxwellian with effective temperature (Raman et al., 1981)

$$T_{1D} = T_{\parallel i} \cos^2 \alpha + T_{\perp i} \sin^2 \alpha, \quad (2)$$

which is generally different from the thermodynamic ion temperature for a bi-Maxwellian

$$T_i = \frac{1}{3} T_{\parallel i} + \frac{2}{3} T_{\perp i}. \quad (3)$$

For toroidal ion distribution functions the ISR theory is far more complex, but the modifications to the spectral shape are only detectable at angles significantly far away from parallel to the magnetic field (Akbari et al., 2017; Winser et al., 1989). For the heating events shown in this study which are characterized by strong  $\vec{V}_i$  flows, anisotropic plasma distributions are a reasonable concern. All data-model comparisons in this study employed high elevation beams with a small aspect angle with respect to the near-vertical magnetic field in the polar cap. Therefore, the measured ion temperatures presented in this work are essentially measurements of the parallel ion temperatures. For either bi-Maxwellian or toroidal distributions that form due to frictional heating, the parallel temperature is expected to be less than the thermodynamic temperature, so the ion temperatures shown in Figures 4 and 6 can be thought of as a lower limit to the

thermodynamic temperature (Akbari et al., 2017). This makes the fact that the modeled temperatures were significantly lower than the observed (lower limit) temperatures all the more significant.

## 5. Conclusion

Joule heating is a significant factor in magnetosphere-ionosphere-thermosphere coupling and energy deposition in the polar cap ionosphere. Using a decade of RISR-N data, we performed a statistical analysis of the conditions under which temperature enhancements were most likely to occur, then attempted to model two notable events with IPWM. On average, the highest ion temperatures were observed under IMF Bz north conditions when the radar was in the noon sector. This is likely due to lobe reconnection driving fast sunwards flows polewards of the cusp which oppose the average neutral wind motion in that region. Data-driven IPWM simulations reproduced some localized heating, but neither the timing nor the magnitude of the temperature enhancements produced by the model matched the dramatic heating events observed in RISR-N data. Calculations using the locally measured ion velocities, however, were able to explain the observations. These results demonstrate that lobe reconnection can produce highly localized fast ion drifts that are very effective at producing frictional heating, and these localized drifts are not well resolved by current global convection pattern mapping techniques. More work is required to determine the origin of mesoscale structures in the polar cap and their impact on energy deposition.

## Data Availability Statement

RISR-N data are available through the SRI International ISR Database at <https://amisr.com/database/>. The code which generates the  $\vec{E} \times \vec{B}$  plasma drift velocities from AMISR data are a python package called “resolvedvelocities”. It is open source and publicly available for contribution at <https://github.com/amisr/resolvedvelocities>, with the version used for this paper permanently available at <http://doi.org/10.5281/zenodo.4451504>. Data for SuperDARN convection maps can be downloaded from the Virginia Tech SuperDARN website at <http://vt.superdarn.org/tiki-index.php?page=ASCIIData>. We would like to thank Xueling Shi, Kevin Sterne, Bharat Kunduri, and Mike Ruohoniemi for assisting us in working with the SuperDARN convection maps. Ovation Prime output was accessed through the open-source python package Ovation Pyme available at <https://github.com/lkilcommons/OvationPyme>. OMNI data were retrieved through SpacePy (Morley et al., 2011). The 5-min-integrated RISR-N database used for the statistical study, specific RISR-N data files used in the event studies, IPWM input and configuration files, and scripts for generating the results and plots shown in this paper have also been made publicly available (<https://doi.org/10.5281/zenodo.4453389>). IPWM output are available at <https://doi.org/10.5281/zenodo.5081167> and <https://doi.org/10.5281/zenodo.5081175>. The analysis code is also available in a configured Resen bucket (Bhatt et al., 2020), also at <https://doi.org/10.5281/zenodo.4453389>.

## Acknowledgments

This work is supported by NSF Grant AGS-1452191 and NASA Grant 80NS-SC21K0458. Additionally, it is based upon work supported by the Resolute Bay Observatory which is a major facility funded by the National Science Foundation through cooperative agreement AGS-1840962 to SRI International.

## References

Aikio, A. T., Cai, L., & Nygrén, T. (2012). Statistical distribution of height-integrated energy exchange rates in the ionosphere. *Journal of Geophysical Research*, 117, A10325. <https://doi.org/10.1029/2012JA018078>

Aikio, A. T., & Selkälä, A. (2009). Statistical properties of joule heating rate, electric field and conductances at high latitudes. *Annales Geophysicae*, 27, 2661–2673. <https://doi.org/10.5194/angeo-27-2661-2009>

Akbari, H., Goodwin, L. V., Swoboda, J., St-Maurice, J.-P., & Semeter, J. L. (2017). Extreme plasma convection and frictional heating of the ionosphere: ISR observations. *Journal of Geophysical Research: Space Physics*, 122, 7581–7598. <https://doi.org/10.1002/2017JA023916>

Bahcivan, H., Tsunoda, R., Nicolls, M., & Heinselman, C. (2010). Initial ionospheric observations made by the new Resolute incoherent scatter radar and comparison to solar wind IMF. *Geophysical Research Letters*, 37, L15103. <https://doi.org/10.1029/2010GL043632>

Bhatt, A., Valentic, T., Reimer, A., Lamarche, L., Reyes, P., & Cosgrove, R. (2020). Reproducible software environment: A tool enabling computational reproducibility in geospace sciences and facilitating collaboration. *Journal of Space Weather and Space Climate*, 10, 12. <https://doi.org/10.1051/swsc/2020011>

Billett, D. D., Wild, J. A., Grocott, A., Aruliah, A. L., Ronksley, A. M., Walach, M.-T., & Lester, M. (2019). Spatially resolved neutral wind response times during high geomagnetic activity above Svalbard. *Journal of Geophysical Research: Space Physics*, 124, 6950–6960. <https://doi.org/10.1029/2019JA026627>

Bristow, W. A., Hampton, D. L., & Otto, A. (2016). High-spatial-resolution velocity measurements derived using local divergence-free fitting of SuperDARN observations. *Journal of Geophysical Research: Space Physics*, 121, 1349–1361. <https://doi.org/10.1002/2015JA021862>

Burke, W. J., Kelley, M. C., Sagalyn, R. C., Smiddy, M., & Lai, S. T. (1979). Polar cap electric field structures with a northwards interplanetary magnetic field. *Geophysical Research Letters*, 6(1), 21–24. <https://doi.org/10.1029/GL006i001p00021>

Cai, L., Aikio, A. T., & Nygrén, T. (2014). Solar wind effect on Joule heating in the high-latitude ionosphere. *Journal of Geophysical Research: Space Physics*, 119, 10440–10455. <https://doi.org/10.1002/2014JA020269>

Chen, Y.-J., & Heelis, R. A. (2018). Mesoscale plasma convection perturbations in the high-latitude ionosphere. *Journal of Geophysical Research: Space Physics*, 123, 7609–7620. <https://doi.org/10.1029/2018JA025716>

Chisham, G., Lester, M., Milan, S. E., Freeman, M. P., Bristow, W. A., Grocott, A., et al. (2007). A decade of the Super Dual Auroral Radar Network (SuperDARN): Scientific achievements, new techniques and future directions. *Surveys in Geophysics*, 28, 33–109. <https://doi.org/10.1007/s10712-007-9017-8>

Chun, F. K., Knipp, D. J., McHarg, M. G., Lacey, J. R., Lu, G., & Emery, B. A. (2002). Joule heating patterns as a function of polar cap index. *Journal of Geophysical Research*, 107(A7), 1119. <https://doi.org/10.1029/2001JA000246>

Clauer, C. R., Xu, Z., Maimaiti, M., Ruohoneimi, J. M., Scales, W., Hartinger, M. D., et al. (2016). Investigation of a rare event where the polar ionospheric reverse convection potential does not saturate during a period of extreme northward IMF solar wind driving. *Journal of Geophysical Research: Space Physics*, 121, 5422–5435. <https://doi.org/10.1002/2016JA022557>

Cousins, E. D. P., & Shepherd, S. G. (2010). A dynamical model of high-latitude convection derived from SuperDARN plasma drift measurements. *Journal of Geophysical Research*, 115, A12329. <https://doi.org/10.1029/2010JA016017>

Cowley, S. W. H. (1983). Interpretation of observed relations between solar wind characteristics and effects at ionospheric altitudes. In Hultqvist, B., & Hagfors, T. (Eds.), *High-latitude space plasma physics* (Vol. 54, pp. 225–249). Boston, MA: Springer. [https://doi.org/10.1007/978-1-4613-3652-5\\_13](https://doi.org/10.1007/978-1-4613-3652-5_13)

Dhadly, M. S., Emmert, J. T., Drob, D. P., Conde, M. G., Aruliah, A., Doornbos, E., et al. (2019). HL-TWiM empirical model of high-latitude upper thermospheric winds. *Journal of Geophysical Research: Space Physics*, 124, 10592–10618. <https://doi.org/10.1029/2019JA027188>

Dungey, J. W. (1961). Interplanetary magnetic field and the auroral zones. *Physical Review Letters*, 6, 47–48. <https://doi.org/10.1103/physrevlett.6.47>

Emmert, J. T., Hernandez, G., Jarvis, M. J., Niciejewski, R. J., Sipler, D. P., & Vennerstrom, S. (2006). Climatologies of nighttime upper thermospheric winds measured by ground-based Fabry-Perot interferometers during geomagnetically quiet conditions: 2. high-latitude circulation and interplanetary magnetic field dependence. *Journal of Geophysical Research*, 111, A12303. <https://doi.org/10.1029/2006JA011949>

Fang, X., Randall, C. E., Lummerzheim, D., Solomon, S. C., Mills, M. J., Marsh, D. R., et al. (2008). Electron impact ionization: A new parameterization for 100 eV to 1 MeV electrons. *Journal of Geophysical Research*, 113, A09311. <https://doi.org/10.1029/2008JA013384>

Farrugia, C. J., Lund, E. J., Sandholt, P. E., Wild, J. A., Coley, S. W. H., Balogh, A., et al. (2004). Pulsed flows at the high-altitude cusp polewards boundary, and associated ionospheric convection and particle signatures, during a Cluster-FAST-SuperDARN-Sondrestrom conjunction under a southwest IMF. *Annales Geophysicae*, 22, 2891–2905. <https://angeo.copernicus.org/articles/22/2891/2004/>

Förster, M., Haaland, S. E., Paschmann, G., Quinn, J. M., Torbert, R. B., Vaith, H., & Kletzing, C. A. (2008). High-latitude plasma convection during northward IMF as derived from in-situ magnetospheric Cluster EDI measurements. *Annales Geophysicae*, 26, 2685–2700. <https://doi.org/10.5194/angeo-26-2685-2008>

Förster, M., Rentz, S., Köhler, W., Liu, H., & Haaland, S. (2008). IMF dependence of high-latitude thermospheric wind pattern derived from CHAMP cross-track measurements. *Annales Geophysicae*, 26, 1581–1595. <https://doi.org/10.5194/angeo-26-1581-2008>

Foster, J. C., St-Maurice, J.-P., & Abreu, V. J. (1983). Joule heating at high latitudes. *Journal of Geophysical Research*, 88(A6), 4885–4896. <https://doi.org/10.1029/JA088ia06p04885>

Fujii, R., Nozawa, S., Buchert, S. C., & Brekke, A. (1999). Statistical characteristics of electromagnetic energy transfer between the magnetosphere, the ionosphere, and the thermosphere. *Journal of Geophysical Research*, 104(A2), 2357–2365. <https://doi.org/10.1029/98JA02750>

Greenwald, R. A., Baker, K. B., Dudeney, J. R., Pinnock, M., Jones, T. B., Thomas, E. C., et al. (1995). DARN/SUPERDARN: A global view of the dynamics of high-latitude convection. *Space Science Reviews*, 71, 761–796. <https://doi.org/10.1007/BF00751350>

Hardy, D. A., Holeman, E. G., Burke, W. J., Gentile, L. C., & Bounar, K. H. (2008). Probability distributions of electron precipitation at high magnetic latitudes. *Journal of Geophysical Research*, 113, A06305. <https://doi.org/10.1029/2007JA012746>

Hardy, D. A., Schmitt, L. K., Gussenhoven, M. S., Yeh, H. C., Schumaker, T. L., Huber, A., & Pantazi, J. (1984). *Precipitating electron and ion detectors (SSJ/4) for the block 5D/flights 6–10 DMSP satellites: Calibration and data presentation* (Tech. Rep. No. AFGL-TR-84-0317 ERP 902). Air Force Geophysics Laboratory. <https://apps.dtic.mil/sti/pdfs/ADA157080.pdf>

Heinselman, C. J., & Nicolls, M. J. (2008). A Bayesian approach to electric field and E-region neutral wind estimation with the Poker Flat Advanced Modular Incoherent Scatter Radar. *Radio Science*, 43, RS5013. <https://doi.org/10.1029/2007RS003805>

Howarth, A., & Yau, A. W. (2008). The effects of IMF and convection on thermal ion outflow in magnetosphere-ionosphere coupling. *Journal of Atmospheric and Solar-Terrestrial Physics*, 70, 2132–2143. <https://doi.org/10.1016/j.jastp.2008.08.008>

Kelly, J., & Heinselman, C. J. (2009). Initial results for Poker Flat Incoherent Scatter Radar (PFISR). *Journal of Atmospheric and Solar-Terrestrial Physics*, 71, 635. <https://doi.org/10.1016/j.jastp.2009.01.009>

Knipp, D. J., Emery, B. A., Engebretson, M., Li, X., McAllister, A. H., Mukai, T., et al. (1998). An overview of the early November 1993 geomagnetic storm. *Journal of Geophysical Research*, 103(A11), 26197–26220. <https://doi.org/10.1029/98JA00762>

Kosch, M. J., Yiu, I., Anderson, C., Tsuda, T., Ogawa, Y., Nozawa, S., et al. (2011). Mesoscale observations of joule heating near an auroral arc and ion-neutral collision frequency in the polar cap E region. *Journal of Geophysical Research*, 116, A05321. <https://doi.org/10.1029/2010JA016015>

Koustov, A. V., Lavoie, D. B., & Varney, R. H. (2016). On the consistency of the SuperDARN radar velocity and E × B plasma drift. *Radio Science*, 51, 1792–1805. <https://doi.org/10.1002/2016RS006134>

Laundal, K. M., & Richmond, A. D. (2017). Magnetic coordinate systems. *Space Science Reviews*, 206, 27–59. <https://doi.org/10.1007/s11214-016-0275-y>

Li, K., Haaland, S., Eriksson, A., André, M., Engwall, E., Wei, Y., et al. (2012). On the ionospheric source region of cold ion outflow. *Geophysical Research Letters*, 39, L18102. <https://doi.org/10.1029/2012GL053297>

Li, K., Haaland, S., Eriksson, A., André, M., Engwall, E., Wei, Y., et al. (2013). Transport of cold ions from the polar ionosphere to the plasma sheet. *Journal of Geophysical Research: Space Physics*, 118, 5467–5477. <https://doi.org/10.1002/jgra.50518>

Lockwood, M., Moen, J., van Eyken, A. P., Davies, J. A., Oksavik, K., & McCrea, I. W. (2005). Motion of the dayside polar cap boundary during substorm cycles: I. Observations of pulses in the magnetopause reconnection rate. *Annales Geophysicae*, 23, 3495–3511. <https://doi.org/10.5194/angeo-23-3495-2005>

Lu, G., Richmond, A. D., Lühr, H., & Paxton, L. (2016). High-latitude energy input and its impact on the thermosphere. *Journal of Geophysical Research Space Physics*, 121, 7108–7124. <https://doi.org/10.1002/2015JA022294>

McHarg, M., Chun, F., Knipp, D., Lu, G., Emery, B., & Ridley, A. (2005). High-latitude Joule heating response to IMF inputs. *Journal of Geophysical Research*, 110, A08309. <https://doi.org/10.1029/2004JA010949>

Moen, J., Lockwood, M., Oksavik, K., Carlson, H. C., Denig, W. F., van Eyken, A. P., & McCrea, I. W. (2004). The dynamics and relationship of precipitation, temperature and convection boundaries in the dayside auroral ionosphere. *Annales Geophysicae*, 22, 1973–1987. <https://doi.org/10.5194/angeo-22-1973-2004>

Moore, T. E., & Horwitz, J. L. (2007). Stellar ablation of planetary atmospheres. *Reviews of Geophysics*, 45, RG3002. <https://doi.org/10.1029/2005RG000194>

Morley, S. K., Koller, J., Welling, D. T., Larsen, B. A., Henderson, M. G., & Niehof, J. T. (2011). SpacePy—A python-based library of tools for the space sciences. In *Proceedings of the 9th python in science conference (scipy 2010)*, Austin, TX. <https://spacepy.github.io/>

Newell, P. T., Sotirelis, T., & Wing, S. (2009). Diffuse, monoenergetic, and broadband aurora: The global precipitation budget. *Journal of Geophysical Research*, 114, A09207. <https://doi.org/10.1029/2009JA014326>

Nishitani, N., Ruohoniemi, J. M., Lester, M., Baker, J. B. H., Koustov, A. V., Shepherd, S. G., et al. (2019). Review of the accomplishments of mid-latitude super dual auroral radar network (SuperDARN) HF radars. *Progress in Earth and Planetary Science*, 6(1), 27. <https://doi.org/10.1186/s40645-019-0270-5>

Olsson, A., Janhunen, P., Ivchenko, N., Blomberg, L. G., & Blomberg, L. G. (2004). Statistics of joule heating in the auroral zone and polar cap using Astrid-2 satellite Poynting flux. *Annales Geophysicae*, 22, 4133–4142. <https://doi.org/10.5194/angeo-22-4133-2004>

Østgaard, N., Germany, G., Stadsnes, J., & Vondrak, R. R. (2002). Energy analysis of substorms based on remote sensing techniques, solar wind measurements, and geomagnetic indices. *Journal of Geophysical Research*, 107(A9), 1233. <https://doi.org/10.1029/2001JA002002>

Palmroth, M., Janhunen, P., Pulkkinen, T. I., Aksnes, A., Lu, G., Østgaard, N., et al. (2005). Assessment of ionosphere Joule heating by GUMICS-4 MHD simulation, AMIE, and satellite-based statistics: Towards a synthesis. *Annales Geophysicae*, 23, 2051–2068. <https://doi.org/10.5194/angeo-23-2051-2005>

Peterson, W. K., Andersson, L., Callahan, B., Elkington, S. R., Winglee, R. W., Scudder, J. D., & Collin, H. L. (2009). Geomagnetic activity dependence of O<sup>+</sup> in transit from the ionosphere. *Journal of Atmospheric and Solar-Terrestrial Physics*, 71, 1623–1629. <https://doi.org/10.1016/j.jastp.2008.11.003>

Picone, J. M., Hedin, A. E., Drob, D. P., & Aikin, A. C. (2002). NRLMSISE-00 empirical model of the atmosphere: Statistical comparisons and scientific issues. *Journal of Geophysical Research*, 107(A12), 1468–1471. <https://doi.org/10.1029/2002JA009430>

Prikryl, P., Provan, G., McWilliams, K. A., & Yeoman, T. K. (2002). Ionospheric cusp flows pulsed by solar wind Alfvén waves. *Annales Geophysicae*, 20, 161–174. <https://doi.org/10.5194/angeo-20-161-2002>

Provan, G., Milan, S. E., Lester, M., Yeoman, T. K., & Khan, H. (2002). Simultaneous observations of the ionospheric footprint of flux transfer events and dispersed ion signatures. *Annales Geophysicae*, 20, 281–287. <https://doi.org/10.5194/angeo-20-281-2002>

Raman, R. S. V., St-Maurice, J.-P., & Ong, R. S. B. (1981). Incoherent scattering of radar waves in the auroral ionosphere. *Journal of Geophysical Research*, 86(A6), 4751–4762. <https://doi.org/10.1029/JA086IA06p04751>

Reiff, P. H., & Heelis, R. A. (1994). Four cells or two? Are force convection cells really necessary? *Journal of Geophysical Research*, 99(A3), 3955–3959. <https://doi.org/10.1029/93JA01992>

Richards, P. G., Woods, T. N., & Peterson, W. K. (2006). HEUVAC: A new high resolution solar EUV proxy model. *Advances in Space Research*, 37, 315–322. <https://doi.org/10.1016/j.asr.2005.06.031>

Richmond, A. D., Lathuillière, C., & Vernerstroem, S. (2003). Winds in the high-latitude lower thermosphere: Dependence on the interplanetary magnetic field. *Journal of Geophysical Research*, 108(A2), 1066. <https://doi.org/10.1029/2002JA009493>

Ruohoniemi, J. M., & Greenwald, R. A. (1996). Statistical patterns of high-latitude convection obtained from Goose Bay HF radar observations. *Journal of Geophysical Research*, 101(A10), 21743–21763. <https://doi.org/10.1029/96JA01584>

Shen, Y., Knudsen, D. J., Burchill, J. K., Howarth, A., Yau, A., Redmon, R. J., et al. (2016). Strong ambipolar-driven ion upflow within the cleft ion fountain during low geomagnetic activity. *Journal of Geophysical Research: Space Physics*, 121(7), 6950–6969. <https://doi.org/10.1002/2016JA022532>

Skjelkvåle, Å., Moen, J., & Carlson, H. C. (2011). On the relationship between flux transfer events, temperature enhancements, and ion upflow events in the cusp ionosphere. *Journal of Geophysical Research*, 116, A10305. <https://doi.org/10.1029/2011JA016480>

St-Maurice, J.-P., & Hanson, W. B. (1982). Ion frictional heating at high latitudes and its possible use for an in situ determination of neutral thermospheric winds and temperatures. *Journal of Geophysical Research*, 87(A9), 7580–7602. <https://doi.org/10.1029/JA087ia09p07580>

St-Maurice, J.-P., & Schunk, R. W. (1979). Ion velocity distributions in the high-latitude ionosphere. *Reviews of Geophysics and Space Physics*, 17(1), 99–134. <https://doi.org/10.1029/RG017001p00099>

St-Maurice, J.-P., & Shunk, R. W. (1977). Auroral ion velocity distributions for a polarization collision model. *Planetary and Space Science*, 25(3), 243–260. [https://doi.org/10.1016/0032-0633\(77\)90135-0](https://doi.org/10.1016/0032-0633(77)90135-0)

Tanskanen, E., Pulkkinen, T. I., & Koskinen, H. E. J. (2002). Substorm energy budget during low and high solar activity: 1997 and 1999 compared. *Journal of Geophysical Research*, 107(A6), 1086. <https://doi.org/10.1029/2001JA900153>

Thayer, J. P., & Semeter, J. (2004). The convergence of magnetospheric energy flux in the polar atmosphere. *Journal of Atmospheric and Solar-Terrestrial Physics*, 66, 807–824. <https://doi.org/10.1016/j.jastp.2004.01.035>

Thayer, J. P., Vickrey, J. F., Heelis, R. A., & Gary, J. B. (1995). Interpretation and modeling of the high-latitude electromagnetic energy flux. *Journal of Geophysical Research*, 100, 19715–19728. <https://doi.org/10.1029/95JA01159>

Thomas, E. G., & Sheperd, S. G. (2018). Statistical patterns of ionospheric convection derived from mid-latitude, high-latitude, and polar SuperDARN HF radar observations. *Journal of Geophysical Research: Space Physics*, 123, 3196–3216. <https://doi.org/10.1002/2018JA025280>

Varney, R. H., Solomon, S. C., & Nicolls, M. J. (2014). Heating of the sunlit polar cap ionosphere by reflected photoelectrons. *Journal of Geophysical Research: Space Physics*, 119, 8660–8684. <https://doi.org/10.1002/2013JA019378>

Varney, R. H., Wiltberger, M., & Lotko, W. (2015). Modeling the interaction between convection and nonthermal ion outflows. *Journal of Geophysical Research: Space Physics*, 120, 2353–2362. <https://doi.org/10.1002/2014JA020769>

Varney, R. H., Wiltberger, M., Zhang, B., Lotko, W., & Lyon, J. (2016). Influence of ion outflow in coupled geospace simulations: 1. Physics-based ion outflow model development and sensitivity study. *Journal of Geophysical Research: Space Physics*, 121, 9671–9687. <https://doi.org/10.1002/2016JA022777>

Wahlund, J.-E., Opgenoorth, H. J., Häggström, I., Winser, K. J., & Jones, G. O. L. (1992). EISCAT observations of topside ionospheric ion outflows during auroral activity: Revisited. *Journal of Geophysical Research*, 97(A3), 3019–3037. <https://doi.org/10.1029/91JA02438>

Winser, K. J., Lockwood, M., Jones, G. O. L., & Suvanto, K. (1989). Observations of nonthermal plasmas at different aspect angles. *Journal of Geophysical Research*, 94(A2), 1439–1449. <https://doi.org/10.1029/JA094IA02p01439>

Yau, A. W., Howarth, A., Pererson, W. K., & Abe, T. (2012). Transport of thermal-energy ionospheric oxygen (O<sup>+</sup>) ions between the ionosphere and the plasma sheet and ring current at quite times preceding magnetic storms. *Journal of Geophysical Research*, 117, A07215. <https://doi.org/10.1029/2012JA017803>

Zhang, B., Brambles, O., Lotko, W., Dunlap-Shohl, W., Smith, R., Wiltberger, M., & Lyon, J. (2013). Predicting the location of polar cusp in the Lyon-Fedder-Mobarry global magnetosphere simulation. *Journal of Geophysical Research: Space Physics*, 118, 6327–6337. <https://doi.org/10.1002/jgra.50565>

Zhang, X. X., Wang, C., Chen, T., Wang, Y. L., Tan, A., Wu, T. S., et al. (2005). Global patterns of Joule heating in the high-latitude ionosphere. *Journal of Geophysical Research*, 110, A12208. <https://doi.org/10.1029/2005JA011222>

Zhu, L., Shunk, R. W., & Sojka, J. J. (1997). Polar cap arcs: A review. *Journal of Atmospheric and Solar-Terrestrial Physics*, 59(10), 1087–1126. <https://doi.org/10.1029/1997JA01771>

Zhu, Q., Deng, Y., Richmond, A., & Maute, A. (2018). Small-scale and mesoscale variabilities in the electric field and particle precipitation and their impacts on Joule heating. *Journal of Geophysical Research: Space Physics*, 123, 9862–9872. <https://doi.org/10.1029/2018JA025771>